



CHORUS

This is the accepted manuscript made available via CHORUS. The article has been published as:

Magnetic field induced Weyl semimetal from Wannier-function-based tight-binding model

John W. Villanova and Kyungwha Park

Phys. Rev. B **98**, 075123 — Published 13 August 2018

DOI: [10.1103/PhysRevB.98.075123](https://doi.org/10.1103/PhysRevB.98.075123)

Magnetic Field Induced Weyl Semimetal from Wannier-Function-based Tight-Binding Model

John W. Villanova* and Kyungwha Park†

Department of Physics, Virginia Tech, Blacksburg, Virginia 24061, USA

(Dated: July 23, 2018)

Abstract

Weyl semimetals (WSMs) have Weyl nodes where conduction and valence bands meet in the absence of inversion or time-reversal symmetry (TRS), or both. The TRS-broken WSM phase can be driven from a topological Dirac semimetal by magnetic field \mathbf{B} or magnetic dopants, considering that Dirac semimetals have degenerate Weyl nodes stabilized by rotational symmetry, i.e. Dirac nodes. Here we develop a Wannier-function-based tight-binding (WF-TB) model to investigate the formation of Weyl nodes and nodal rings induced by \mathbf{B} field in the topological Dirac semimetal Na_3Bi . The field is applied along the rotational axis. So far, studies of \mathbf{B} field induced WSMs have been limited to cases with effective models. Remarkably, our study based on the WF-TB model shows that upon \mathbf{B} field each Dirac node is split into *four* separate Weyl nodes along the rotational axis near the Fermi level; two nodes with Chern number ± 1 (single Weyl nodes) and two with Chern number ± 2 (double Weyl nodes). This result is in contrast to the common belief that each Dirac node consists of only two single Weyl nodes with opposite chirality. In the context of the 4×4 effective models, the existence of double Weyl nodes ensures nonzero cubic terms in momentum. We examine the evolution of Fermi arcs at a side surface as a function of chemical potential. The number of Fermi arcs at a given chemical potential is consistent with the corresponding Fermi surface Chern numbers. Our study also reveals the existence of nodal rings in the mirror plane near the Fermi level upon \mathbf{B} field. These nodal rings persist with spin-orbit coupling. Our WF-TB model can be used to compute interesting features such as anomalous Hall and thermal conductivities, and our findings can be applied to other topological Dirac semimetals like Cd_3As_2 .

I. INTRODUCTION

In Weyl semimetals (WSMs), bulk conduction and valence bands touch at an even number of points near the Fermi level, called Weyl nodes, which are topologically protected by conserved crystal momentum^{1,2}. The WSM phase occurs when inversion symmetry (IS) or time reversal symmetry (TRS) is broken or both. A non-zero Chern number is associated with each Weyl node, and it also dictates the number of open Fermi-arc surface states. Since early theoretical proposals of WSM in iridates², HgCr_2Se_4 ^{3,4}, and TaAs^{5,6}, experimental observation of Weyl nodes in IS-broken WSMs TaAs family⁷⁻⁹ has stimulated the field. In addition to Weyl nodes with Dirac dispersion in three orthogonal directions (single Weyl nodes, Chern number ± 1), various types of Weyl nodes were proposed and observed. To name a few, double (triple) Weyl nodes with Chern numbers ± 2 (± 3) are associated with quadratic (cubic) dispersion in the plane orthogonal to the Weyl node separation axis^{3,4,10,11}; type-II Weyl nodes^{12,13} are realized when conduction and valence bands meet with the same sign of slope such that electron and hole pockets are formed near the Fermi level. WSMs are expected to show interesting phenomena arising from Berry curvature, such as the chiral magnetic effect¹⁴⁻¹⁶, anomalous Hall conductivity and Nernst effect^{17,18}, and unique quantum oscillations^{19,20}.

Mostly IS-broken WSMs have been experimentally well characterized, with dozens of Weyl nodes found near the Fermi level, and often off symmetry lines or planes in momentum \mathbf{k} space^{5,8,9}. Experimental studies of TRS-broken WSMs based on magnetic materials are in debate due to material stability or difficulty in identification of magnetic ordering²¹. (Here a strict definition of WSMs is applied where there are no other trivial bands than the bands forming Weyl nodes near the Fermi level.) A recent study proposed that if doped TRS-broken WSMs with IS can realize a superconducting state with translational symmetry, then the superconducting state must have an odd-parity, spin-triplet pair potential²². However, such a scenario is not guaranteed in doped IS-broken WSMs.

One way to induce the TRS-broken WSM phase is to apply a magnetic field \mathbf{B} or insert magnetic dopants in topological Dirac semimetals (DSMs). Despite TRS and IS, topological DSMs have degenerate Weyl nodes with opposite chirality, i.e. Dirac nodes, which are protected by rotational symmetry²³. Topological DSMs Na_3Bi and Cd_3As_2 were experimentally confirmed to have only two Dirac nodes well separated along the rotational symmetry

axis^{24,25}. Thus, breaking TRS would generate a much smaller number of Weyl nodes compared to IS-broken WSMs. It is commonly believed that each Dirac node would split into two Weyl nodes of opposite chirality upon \mathbf{B} field. This arises from studies of the 4×4 effective model keeping only up to quadratic terms in k ^{17,18,23,26,27}. Although a possibility of higher-order terms was discussed in the effective model^{26,28,29}, the existence and strength of such terms have not been investigated before. So far there are no first-principles-based studies of \mathbf{B} field induced WSMs.

In order to investigate topological properties of \mathbf{B} field induced WSMs beyond simple effective models, we develop a Wannier-function-based tight-binding (WF-TB) model for topological DSM Na₃Bi with \mathbf{B} field applied along the rotational axis. The electronic structure of bulk Na₃Bi is first calculated from density-functional theory (DFT) without spin-orbit coupling (SOC) or \mathbf{B} field. Atom-centered Wannier functions (WFs) are generated from the electronic structure, and we then construct a WF-TB model by separately adding atomic-like SOC and a Zeeman energy. Landau levels or Peierls phases are not considered in our WF-TB model. The band structure calculated from the WF-TB model still respects C_3 and 6_3 (screw) symmetries and mirror symmetry (σ_h) upon \mathbf{B} field. We avoid maximally-localized WFs in our construction of the WF-TB model. Topological obstruction^{30,31} is not relevant in our WF-TB model since unoccupied bands are included. For example, in topological insulators and semimetals, WF-TB models have been successfully used to investigate topological invariants and other properties^{5,32,33}.

From the WF-TB model, we find that upon \mathbf{B} field each Dirac node is split into *four* separate Weyl nodes along the rotational axis near the Fermi level. Two of the nodes have Chern number of ± 1 (single Weyl nodes), while the other two nodes have Chern number of ± 2 (double Weyl nodes). This result differs from the common belief that each Dirac node consists of two Weyl nodes of opposite chirality, which is true only when higher-order terms like cubic terms are ignored in the 4×4 effective model. Our calculated Chern numbers associated with the double Weyl nodes unambiguously reveals the existence of the higher-order terms in momentum. We further examine the evolution of Fermi arcs at a side surface as a function of chemical potential, finding that the number of Fermi arcs is consistent with the calculated Chern numbers associated with the Weyl nodes. This analysis corroborates our findings of the double Weyl nodes. In addition, our study reveals that with \mathbf{B} field there are nodal rings in the mirror plane, i.e. ab plane, near the Fermi level. These nodal rings

persist with SOC, in contrast to most proposed nodal ring semimetals where the nodal rings are gapped by SOC except for a few \mathbf{k} points. Our WF-TB model with \mathbf{B} field can be used to compute interesting features arising from Berry curvature such as anomalous Hall and thermal conductivities. Our findings can be applied to other topological Dirac semimetals like Cd_3As_2 .

We present crystal structure and symmetries of Na_3Bi in Sec. II and the detailed procedure of constructing the WF-TB model in Sec. III. Then in Sec. IV we discuss the WF-TB model calculated band structure, the calculated Chern numbers of the Weyl nodes, the calculated nodal rings, and the evolution of the Fermi arcs versus chemical potential. We conclude in Sec. V.

II. CRYSTAL STRUCTURE AND SYMMETRIES OF Na_3Bi

We consider bulk Na_3Bi in space group $P6_3/mmc$ (No. 194) with experimental lattice constants of $a = 5.448 \text{ \AA}$ and $c = 9.655 \text{ \AA}$ ²⁶ and no geometry relaxation is performed within DFT. There are two inequivalent Na sites, 2b and 4f, with $z = 0.5827$ for the latter in Wyckoff convention, and these are shown in Fig. 1 in blue and green, respectively. There is one inequivalent Bi site, 2c in Wyckoff convention shown in gold in Fig. 1. The site symmetries of 2b, 4f, and 2c sites are D_{3h} , C_{3v} , and D_{3h} , respectively. The primitive unit cell in real space consists of six Na atoms and two Bi atoms, and an associated first Brillouin zone (BZ) is shown in Fig. 1(c). The bulk crystal has inversion symmetry, C_3 rotational and 6_3 screw symmetries about the c axis (or z axis), and seven mirror planes (the single horizontal xy plane, yz -mirror, and xz -glide, as well as the four other planes related to the latter two of these species by rotational symmetry). Note that our x and y coordinates are reversed from those in Ref. 26. Henceforth, we refer to the global primitive cell coordinates as unprimed and the local $(1\bar{2}0)$ cell coordinates as primed. For convenience, we use the $z' \perp (1\bar{2}0)$ non-primitive unit cell for all that follows, unless specified otherwise. The non-primitive unit cell has a rectangular shape and its dimension is $9.436 \times 9.655 \times 5.448 \text{ \AA}^3$. The volume of the non-primitive unit cell is twice that of the primitive unit cell. Note that the non-primitive cell is not expanded along the crystal c -axis. Here the unit vectors in the local coordinates are related to those in the global coordinates as follows: $(\hat{x}', \hat{y}', \hat{z}') \rightarrow (-\hat{y}, \hat{z}, -\hat{x})$. We consider a side surface $(1\bar{2}0)$ for the study of Fermi-arc surface states in Sec. IV.D and

E. The reason we use the non-primitive unit cell will be discussed in Sec. III.B.

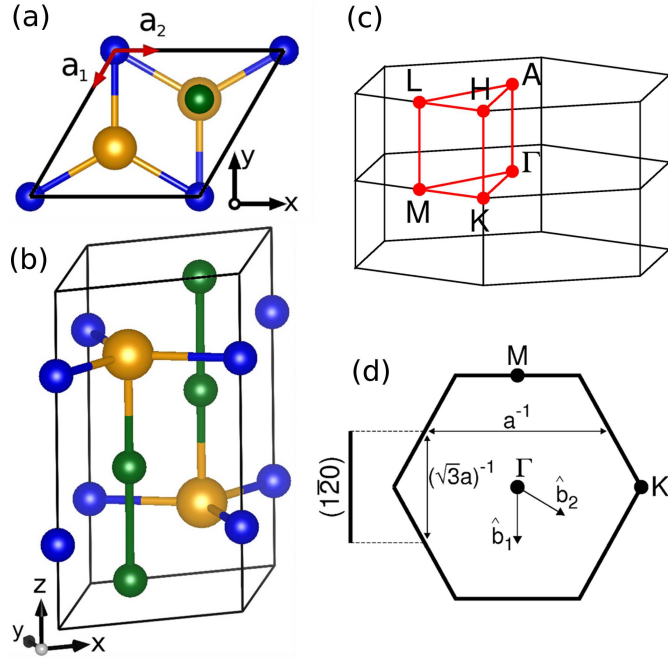


FIG. 1: (Color online) (a) Top-down view of the primitive (001) unit cell of Na_3Bi which crystallizes in the $P6_3/mmc$ hexagonal structure. Bi atoms are orange and Na atoms are blue (Wyckoff site 2b) and green (4f). (b) The primitive unit cell at a slight perspective angle. The in-plane lattice vectors are shown in (a). (c) A first Brillouin zone (BZ) associated with the primitive (001) unit cell. (d) Top-down view of the primitive cell first BZ showing the projection onto the $(1\bar{2}0)$ plane. (Panels (a), (b), and (d) are used with permission, copyright 2017 American Chemical Society³⁴.)

III. CONSTRUCTION OF WANNIER-FUNCTION-BASED TIGHT-BINDING MODEL

We first calculate the electronic structure of bulk Na_3Bi without SOC and \mathbf{B} field by using DFT codes VASP³⁵ and QUANTUM ESPRESSO (QE)³⁶. Next we generate the WFs from the DFT-calculated band structure using WANNIER90³⁷. Then we construct a tight-binding model from the WFs and add atomic-like SOC and Zeeman energy to the tight-binding model.

A. Initial DFT calculations

We perform the *ab-initio* calculations using QE³⁶ within the Perdew-Burke-Ernzerhof (PBE) generalized-gradient approximation (GGA)^{38,39} for the exchange-correlation functional without SOC. We use the Na.pbe-spn-kjpaw_psl.0.2.UPF and Bi.pbe-dn-kjpaw_psl.0.2.2.UPF projector augmented wave (PAW) pseudopotentials⁴⁰ with an energy cutoff of 50 Ry and smearing of 0.001 Ry. We consider bulk Na₃Bi with the experimental lattice constants²⁶ without further relaxation. We use the $z' \perp (1\bar{2}0)$ non-primitive unit cell for all that follows other than the band structure calculation. We use an $11 \times 11 \times 7$ Monkhorst-Pack k -point mesh in the former case and a $7 \times 7 \times 15$ mesh in the latter case. In both k -point samplings, the Γ point is included. We also calculate the electronic structure by using VASP³⁵ with the PBE-GGA and PAW pseudopotentials in the absence of SOC and with a $11 \times 11 \times 5$ mesh. We use an energy cutoff of 250 eV and smearing of 0.05 eV. We find excellent agreement between the QE-calculated and the VASP-calculated electronic structures, which justifies our choices of the PAW pseudopotentials⁴⁰ used in QE.

B. Generation of the Wannier functions

A Wannier function, $|\mathbf{r} - \mathbf{R}', n\rangle$, centered at position \mathbf{R}' in real space is a Fourier transform of Bloch states, $|\psi_{nk}(\mathbf{r})\rangle$, over the \mathbf{k} space, where n is a band index. The Bloch states can be written as $e^{i\mathbf{k}\cdot\mathbf{r}}u_{n\mathbf{k}}(\mathbf{r})$, where $u_{n\mathbf{k}}(\mathbf{r})$ denotes a lattice-periodic function.

$$|\mathbf{r} - \mathbf{R}', n\rangle = \frac{V}{(2\pi)^3} \int d^3k e^{-i\mathbf{k}\cdot\mathbf{R}'} |\psi_{nk}(\mathbf{r})\rangle, \quad (1)$$

$$|\psi_{nk}(\mathbf{r})\rangle = \sum_{\mathbf{R}'} e^{i\mathbf{k}\cdot\mathbf{R}'} |\mathbf{r} - \mathbf{R}', n\rangle, \quad (2)$$

where V is the volume of the first BZ. Although the concept of Wannier functions was developed very early⁴¹, their practical usage has rapidly developed in the past twenty years since two bottlenecks were removed by Marzari, Vanderbilt, and collaborators^{42,43}. The first difficulty was non-uniqueness of WFs due to gauge freedom, which was resolved by searching for maximally localized Wannier functions⁴². The second bottleneck was dealing with cases in which the set of bands of interest is not separated from a larger set of bands by a gap at every k point, as is the case in metals. This was solved by minimizing the gauge invariant part of the spread functional⁴³. These features are implemented in WANNIER90 code³⁷.

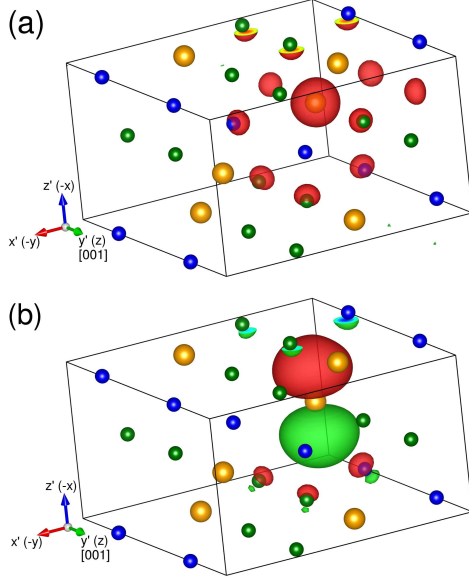


FIG. 2: (Color online) (a) Wannier function corresponding to an s -orbital, and (b) Wannier function corresponding to a $p_{z'}$ -orbital in the non-primitive unit cell. An isosurface level of $3 \text{ eV}/\text{\AA}^3$ is chosen in both panels. Bi atoms are orange and Na atoms are blue (Wyckoff site 2b) and green (4f). Green Na atoms are vertically oriented relative to the Bi atoms in the primitive hexagonal cell.

Before presenting our WF generation, let us discuss several criteria that the WFs must satisfy in our WF-TB model. First, the WF-TB model must reproduce the DFT-calculated band structure near the Fermi level with and without SOC. Some occupied and unoccupied bands near the Fermi levels are needed to investigate the Dirac and Weyl nodes. Second, the band structure obtained from the WF-TB model must respect inherent crystal symmetries with and without \mathbf{B} field. There is a topological obstruction^{30,31,44} to the construction of (maximally-localized) WFs for Chern insulators and topological insulators when only occupied bands are considered. In addition, maximally localized WFs tend to break crystal symmetries, while projected atomic WFs (without maximal localization) respect crystal symmetries³². Thus, we carry out only the disentanglement procedure by minimizing the gauge-invariant part of the spread functional Ω_I . The definition of Ω_I can be found from Ref. 43. Third, the Wannier centers should be at the atomic centers. Fourth, the WFs must be either very close to pure atomic orbitals or a linear combination of them. The third and fourth criteria are required because we add the atomic-like SOC and a Zeeman energy term. Fifth, the spread functional of each WF must not be too large to exceed the size of

the home cell. Sixth, a small number of WFs is desirable in order to reduce the size of the Hamiltonian matrix.

In order to first construct the SOC-free WF-TB model, we start with an initial set of 16 projected atomic orbitals, g_j , comprising s -, $p_{x'}$ -, $p_{y'}$ -, and $p_{z'}$ -orbitals centered at the four Bi atoms in the $z' \perp (1\bar{2}0)$ unit cell. Using the DFT-calculated Bloch eigenvalues and eigenstates, we compute the overlap matrix, $M_{mn}^{\mathbf{k},\mathbf{b}} = \langle u_{m\mathbf{k}} | u_{n\mathbf{k}+\mathbf{b}} \rangle$, and projection matrix, $A_{mj}^{(\mathbf{k})} = \langle \psi_{m\mathbf{k}} | g_j \rangle$, at each DFT-sampled k point by using WANNIER90³⁷. Here m and n are indices of the Bloch states or bands, \mathbf{b} is a vector between two neighboring k points, and j is the WF index. Then we apply only the disentanglement procedure within the outer energy window $[-3.86, 5.44]$ eV with respect to the Fermi level. In this energy window, the number of Bloch bands ($27 \leq N_b(\mathbf{k}) \leq 34$) is much greater than the number of the WFs, where the number of occupied bands is 12 and the total number of Bloch bands depends on \mathbf{k} . We find that the generated WFs have only real components and that the WFs are close to pure atomic orbitals, as shown in Fig. 2. In the case of the projected s -orbital WFs, there are small contributions from the neighboring Na sites. This does not affect our implementation of SOC since the s -orbital WFs do not contribute to SOC. The Wannier centers are at the atomic centers within the order of 0.001 Å for the p -orbital WFs and 0.01 Å for the s -orbital WFs. The spreads of the individual WFs as well as the Wannier centers are listed in Table I. The p -orbital WFs are well localized, whereas the s -orbital WFs are substantially delocalized but their spreads remain within the home non-primitive unit cell. Such spreads could be the reason we obtain a better set of WFs when we increase the unit cell size in real space, compared to the case of using a primitive unit cell. Here a “better set” of WFs means improved agreement with the DFT-calculated band structure while respecting the crystal symmetries. A similar effect has been discussed for topological insulators⁴⁵. With the generated WFs, the gauge-invariant part of the spread functional Ω_I is 84.69 Å², and the diagonal and off-diagonal non-invariant part of the spread functionals Ω_D and Ω_{OD} are 0.15 and 19.21 Å², respectively. We also check that matrix $A^{\dagger(\mathbf{k})}A^{(\mathbf{k})}$ is not singular at any \mathbf{k} points for our choice of the initial set g_j .

TABLE I: Cartesian positions (\AA) of the WFs for the $(1\bar{2}0)$ cell with their spreads. The atomic positions are listed at the top of the table for ease of comparison. All coordinates are *local*.

Atom	Orbital	x'	y'	z'	Spread (\AA^2)
Bi 1		1.57270	2.41375	2.72400	
Bi 2		3.14540	7.24125	0.00000	
Bi 3		6.29081	2.41375	0.00000	
Bi 4		7.86351	7.24125	2.72400	
1	s	1.53021	2.41377	2.72400	13.30
2	s	3.18791	7.24123	0.00000	13.30
1	$p_{z'}$	1.56990	2.41375	2.72400	4.36
1	$p_{x'}$	1.57225	2.41375	2.72400	4.36
1	$p_{y'}$	1.56931	2.41375	2.72400	3.99
2	$p_{z'}$	3.14821	7.24125	0.00000	4.36
2	$p_{x'}$	3.14587	7.24125	0.00000	4.36
2	$p_{y'}$	3.14880	7.24125	0.00000	3.99
3	s	6.24840	2.41377	0.00000	13.30
4	s	7.90603	7.24123	2.72400	13.30
3	$p_{z'}$	6.28801	2.41375	0.00000	4.36
3	$p_{x'}$	6.29034	2.41375	0.00000	4.36
3	$p_{y'}$	6.28742	2.41375	0.00000	3.99
4	$p_{z'}$	7.86632	7.24125	2.72400	4.36
4	$p_{x'}$	7.86398	7.24125	2.72400	4.36
4	$p_{y'}$	7.86691	7.24125	2.72400	3.99

C. Spin-free Hamiltonian

Now we construct the spin-free WF-TB model, by using the generated WFs, $|\mathbf{R} + \mathbf{s}_\beta\rangle$, centered at $\mathbf{R} + \mathbf{s}_\beta$, where \mathbf{R} are the lattice vectors and \mathbf{s}_β denote the sites of orbital β

($\beta=1,\dots,16$). The spin-free Hamiltonian matrix \mathcal{H}_0 reads

$$\mathcal{H}_{0,\alpha\beta}(\mathbf{k}) = \langle \psi_{\mathbf{k},\alpha} | \mathcal{H}_0 | \psi_{\mathbf{k},\beta} \rangle, \quad (3)$$

$$= \sum_{\mathbf{R}} e^{-i\mathbf{k}\cdot(\mathbf{R}+\mathbf{s}_\alpha-\mathbf{s}_\beta)} t_{\alpha\beta}(\mathbf{R}-\mathbf{0}), \quad (4)$$

$$t_{\alpha\beta}(\mathbf{R}-\mathbf{0}) = \langle \mathbf{R} + \mathbf{s}_\alpha | \mathcal{H}_0 | \mathbf{0} + \mathbf{s}_\beta \rangle, \quad (5)$$

where $t_{\alpha\beta}(\mathbf{R}-\mathbf{0})$ is a hopping or tunneling parameter from orbital β at site \mathbf{s}_β in the home cell at $\mathbf{R} = \mathbf{0}$ to orbital α at site \mathbf{s}_α in the unit cell located at \mathbf{R} . Note that we have four different Bi sites within the non-primitive unit cell. The factor $e^{-i\mathbf{k}\cdot(\mathbf{s}_\alpha-\mathbf{s}_\beta)}$ in Eq. (4) can be absorbed into a new basis set.

D. Addition of spin-orbit coupling and Zeeman term

Since the atom-centered Wannier functions are very close to pure states of the orbitals we project onto, on-site SOC is added to the home-cell terms directly. The matrix form of SOC in the basis set of $\{|s, \uparrow\rangle, |p_{z'}, \uparrow\rangle, |p_{x'}, \uparrow\rangle, |p_{y'}, \uparrow\rangle, |s, \downarrow\rangle, |p_{z'}, \downarrow\rangle, |p_{x'}, \downarrow\rangle, |p_{y'}, \downarrow\rangle\}$ for a single Bi atom is

$$\mathcal{H}_{SOC} = \lambda \mathbf{L} \cdot \boldsymbol{\sigma} = \frac{\lambda}{2} \begin{pmatrix} 0 & 0 & 0 & 0 & 0 & 0 & 0 & 0 \\ 0 & 0 & 0 & 0 & 0 & 0 & -1 & i \\ 0 & 0 & 0 & -i & 0 & 1 & 0 & 0 \\ 0 & 0 & i & 0 & 0 & -i & 0 & 0 \\ 0 & 0 & 0 & 0 & 0 & 0 & 0 & 0 \\ 0 & 0 & 1 & i & 0 & 0 & 0 & 0 \\ 0 & -1 & 0 & 0 & 0 & 0 & 0 & i \\ 0 & -i & 0 & 0 & 0 & 0 & -i & 0 \end{pmatrix}, \quad (6)$$

where λ is the SOC parameter, \mathbf{L} is the orbital angular momentum, and $\boldsymbol{\sigma}$ represent Pauli spin matrices. With our generated WFs, we now have a 32×32 matrix \mathcal{H}_{SOC} since there are four Bi sites per non-primitive unit cell. We find that $\lambda = 1.165$ eV reproduces the DFT band structure around the Fermi level the best, which is to be favorably compared to $\lambda_{\text{Bi}} = 1.25$ eV⁴⁶.

We add the magnetic field as a Zeeman term $\mathcal{H}_Z = \tilde{g}\mu_B(\mathbf{L} + 2\mathbf{S}) \cdot \mathbf{B}$, where μ_B is Bohr magneton and \mathbf{S} is the spin angular momentum. For a free electron, $\tilde{g} = 1$. We do not

include Peierls phases in the hopping parameters $t_{\alpha\beta}$. The total Hamiltonian for the WF-TB model is $\mathcal{H} = \mathcal{H}_0 + \mathcal{H}_{SOC} + \mathcal{H}_Z$. For the results presented through the rest of this work, we consider $\tilde{g}\mu_B B_z = 0.025$ eV, unless specified otherwise. The experimentally realized Dirac semimetals exhibit large g-factors, with $g \approx 20$ in Na_3Bi ⁴⁷ and $g \approx 40$ in Cd_3As_2 ⁴⁸, and the magnetic field strength that we consider is experimentally achievable. However, our findings would *not* qualitatively change with the field strength if the magnetic field is not extremely high. For example, the number of the Weyl nodes near the Fermi level, the Chern numbers associated with the Weyl nodes, the existence of the cubic terms in k in the 4×4 effective model, and the existence of at least one nodal ring, do not change when $\tilde{g}\mu_B B_z$ is less than 0.05 eV. We choose the particular value of \mathbf{B} field since the splitting of each Dirac node is more visible and easier to analyze.

IV. RESULTS AND DISCUSSION

A. Calculated band structure and symmetry

We check that our WF-TB model reproduces the first-principles band structure without SOC. Figure 3(a) shows the WF-TB-calculated band structure overlain with the VASP-calculated one in the absence of SOC. Except for the band-folding, there is excellent agreement between the two band structures over a wide range of energies, approximately within $[-4.0, 1.0]$ eV with respect to the Fermi level. In the Appendix, we show both the VASP-calculated and the WF-TB-calculated band structures in the non-primitive unit cell for a comparison with band-folding. Especially, the band structure near the Dirac node along the A- Γ direction is well reproduced from the WF-TB model Hamiltonian. We note that the VASP-calculated band structure is identical to the QE-calculated one. In the vicinity of the Dirac node, the QE-calculated band structure demonstrates that the two crossing bands, without SOC, consist of one band with Na s , Bi s , and Bi p_z orbital characters, and the other band with Bi p_x and p_y orbital characters (in the global coordinates). The composition of the orbital characteristics is shown in Fig. 4. The contribution of the Na s orbital is hardly larger than the contribution of the Bi s plus p_z orbitals along the A- Γ direction. This fact, along with the observation that the resultant WFs comport with our six criteria, justifies our choice of the initial set, g_j .

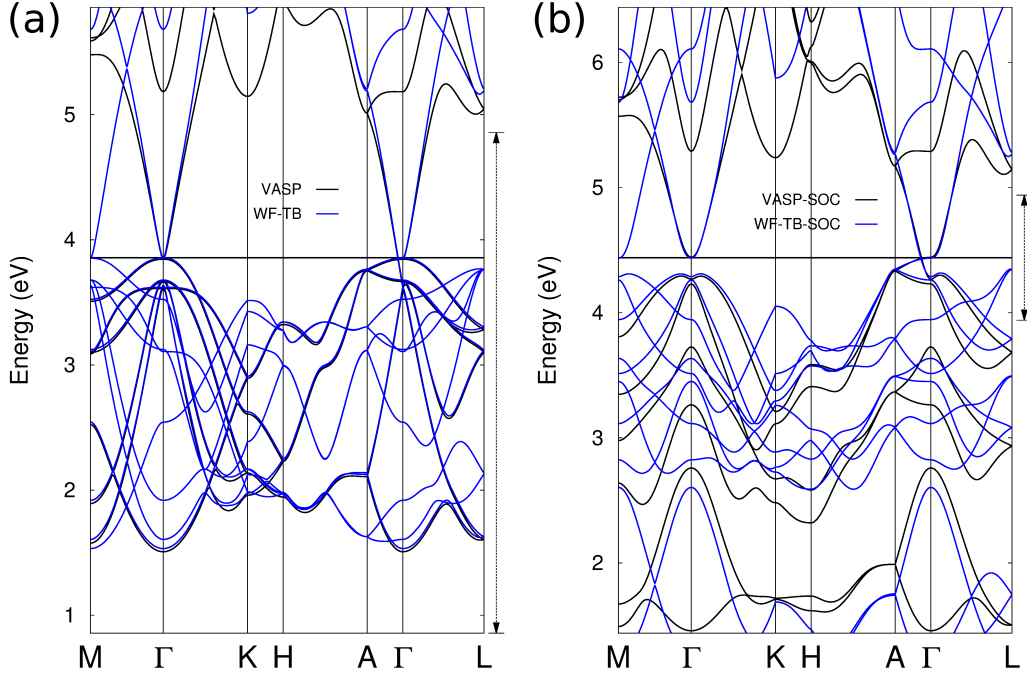


FIG. 3: (Color online) (a) Comparison of the bulk band structure without SOC of Na_3Bi , using VASP with the primitive unit cell versus the WF-TB Hamiltonian with the non-primitive unit cell. (b) Likewise with SOC, with the Dirac node circled. In both cases the band-folding is apparent, especially where the $(1\bar{2}0)$ -BZ ends halfway along $\text{M}\Gamma$. The vertical arrows draw the eye to the region of excellent agreement referenced in the text. The horizontal solid lines in the middle in (a) and (b) indicate the Fermi levels. Here (a) and (b) are without \mathbf{B} field.

Now we diagonalize the 32×32 matrix, $\mathcal{H}_0 + \mathcal{H}_{\text{SOC}}$, with the same interpolated k points, in order to check if our WF-TB model reproduces the first-principles band structure with SOC. As shown in Fig. 3(b), with SOC, we also find excellent agreement between the WF-TB- and VASP-calculated band structures near the Fermi level. See also the band structures in the non-primitive unit cell in the Appendix for a comparison with band-folding. The Dirac node from the WF-TB model is found to be at 0.08785 \AA^{-1} , which agrees well with the location of the DFT-calculated Dirac node. Furthermore, we investigate the symmetry of the WF-TB-calculated band structure by computing the constant energy contours of the top valence band in the global- xy plane. With and without magnetic field, we find sixfold rotational symmetry (Fig. 5). This result is consistent with the 6_3 screw and σ_h (mirror symmetry about the xy or $z'x'$ plane) crystal symmetries, adding further credence to the

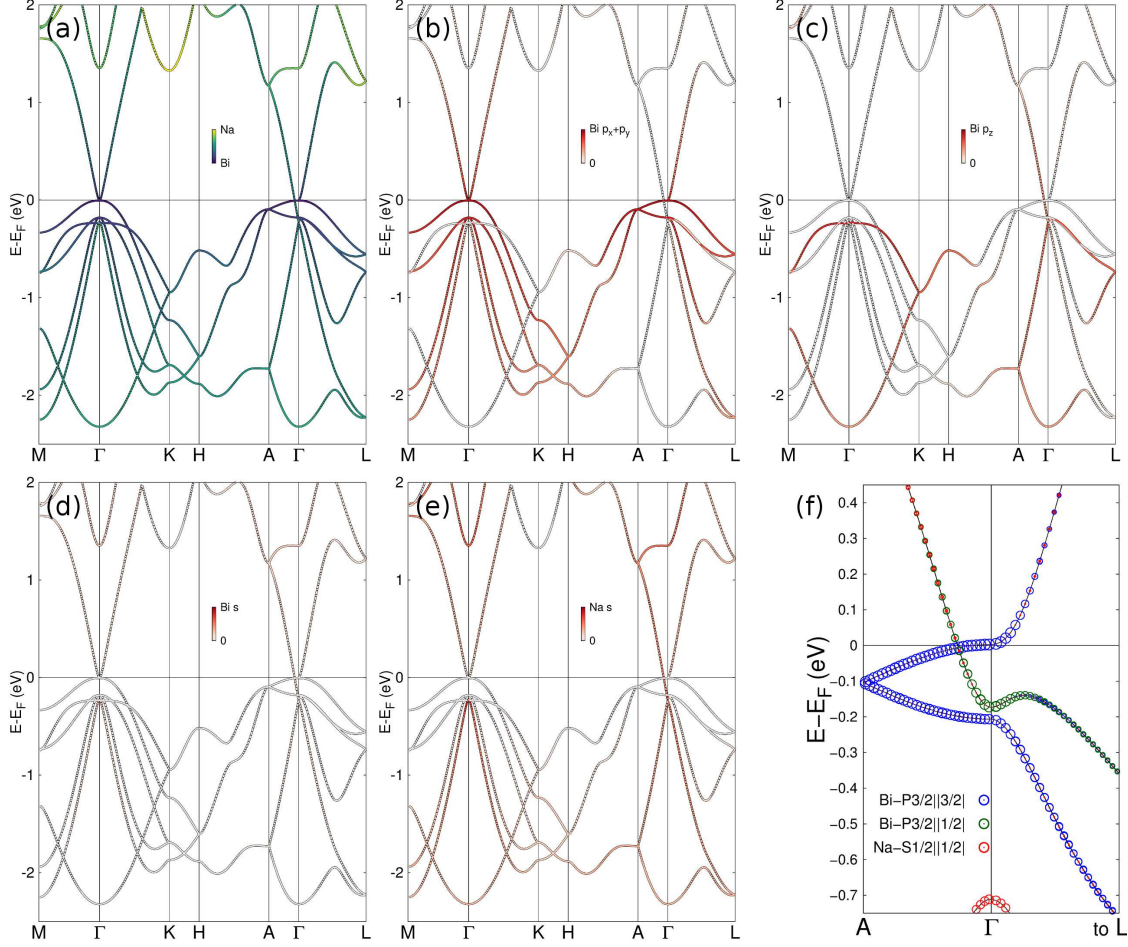


FIG. 4: (Color online) (a) QE-calculated band structure without SOC colored for the contributions of Na and Bi states. (b-e) QE-calculated band structure without SOC colored for the fraction of the contribution of each orbital at each k point, (b) Bi in-plane p_x and p_y orbitals, (c) Bi p_z , (d) Bi s , and (e) Na s . (f) QE-calculated band structure *with* SOC, demonstrating the Dirac node as a crossing of two doubly-degenerate bands with different rotational eigenvalues, $|j_z| = 3/2$ (blue) and $|j_z| = 1/2$ (red and green). All cases use the primitive unit cell without \mathbf{B} field.

validity of the WF-TB model. Note that we carefully check all aspects of the forthcoming results near the Fermi level, confirming that those results are not influenced by the band folding.

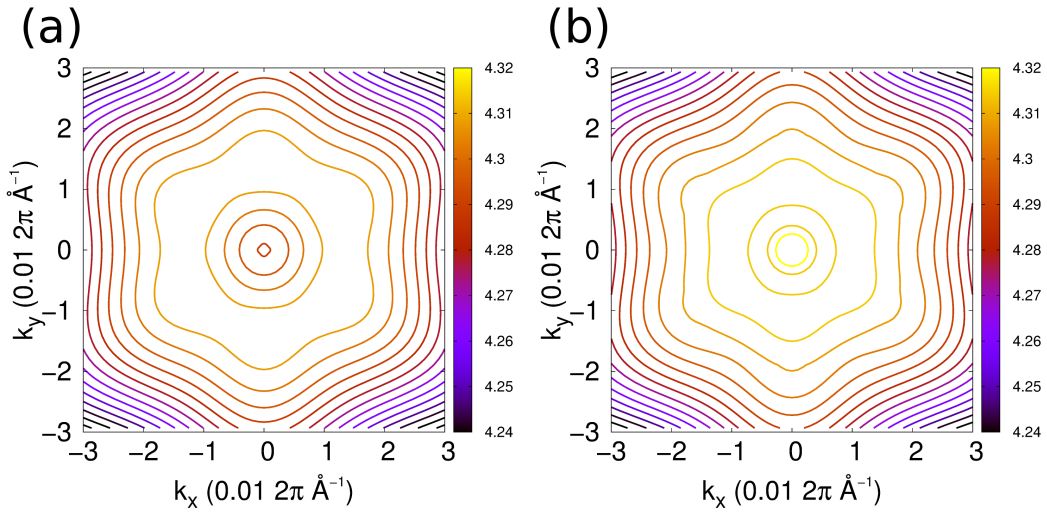


FIG. 5: (Color online) (a) Constant energy contours of the top valence band in the $k_z=0$ plane as calculated from the WF-TB model for the $(\bar{1}20)$ cell in the absence of the magnetic field. (b) Constant energy contours of the top valence band in the $k_z=0$ plane as calculated from the WF-TB model of the $(\bar{1}20)$ cell with an applied magnetic field of 25 meV, exhibiting the hexagonal symmetry. In both panels, SOC is included and the colorscale is for the energy (eV). The Fermi level in (a) and (b) is 4.44 eV.

B. Splitting Dirac Nodes via Magnetic Field: Single and Double Weyl nodes

We apply a magnetic field along the 6_3 screw axis (c axis) of Na_3Bi , finding that each Dirac node [Fig. 6(a)] splits into four separate Weyl nodes along the c axis. Figure 6(b) and (c) shows the development of the four Weyl nodes along the c axis in the half-BZ upon \mathbf{B} field. Between these values of \mathbf{B} field, the number of field-induced Weyl nodes does not change and nor do the chiralities of the nodes. We henceforth present only the result for $\tilde{g}\mu_B B_z=0.025$ eV, though we note that there is still no qualitative change in the results even for larger fields $\tilde{g}\mu_B B_z < 0.05$ eV. Each Weyl node is labeled such that W_n denotes a band crossing point between bands n and $n+1$. When there are multiple crossing points arising from bands n and $n+1$, an additional index is included right next to the band index. In order to determine the chiral charge of the Weyl nodes, we first calculate the Berry curvature of the Bloch bands obtained from our generated WF-TB model including the SOC and Zeeman

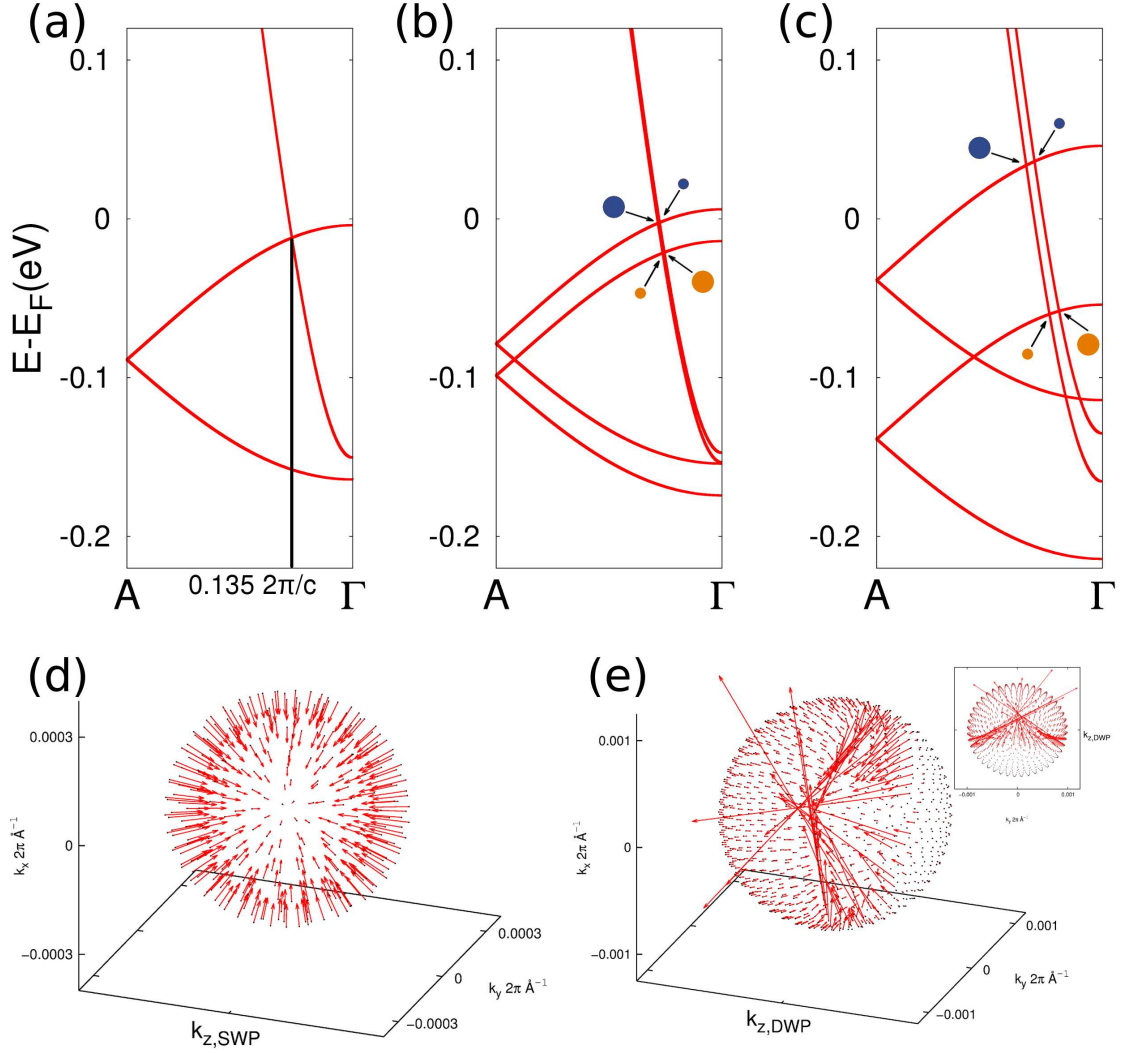


FIG. 6: (Color online) Band structure of Na_3Bi along the rotation axis (a) without \mathbf{B} field, (b) with $\tilde{g}\mu_B B_z = 5$ meV, and (c) with $\tilde{g}\mu_B B_z = 25$ meV. In (a), the location of the Dirac node is marked. In (b) and (c) the positive (negative) chirality Weyl nodes are noted in orange (blue) circles, with the small (large) circles meaning Chern numbers of ± 1 (± 2). (d) Berry curvature in the vicinity of a single Weyl point W_{25} with chiral charge of -1 . The “anti-hedgehog” monopole shape is apparent. (e) Berry curvature in the vicinity of a double Weyl point $W_{24,a}$ with chiral charge of -2 . The “anti-hedgehog” shape is quite different, with almost all of the Berry curvature arising on a chord of the sphere. The inset shows the projection of the Berry curvature of (e) onto the $k_z = 0$ plane, showing the chord which is almost along an equator of the sphere.

term, by using WANNIER TOOLS⁴⁹. The Berry curvature of band n in momentum space, $\mathbf{\Omega}_n(\mathbf{k})$, is defined to be $\nabla_{\mathbf{k}} \times \mathbf{A}_n(\mathbf{k})$, where $\mathbf{A}_n(\mathbf{k}) = i\langle u_{n\mathbf{k}} | \nabla_{\mathbf{k}} u_{n\mathbf{k}} \rangle$. Defining $\mathcal{H}_\alpha \equiv \partial\mathcal{H}/\partial k_\alpha$ and within the space represented by the WFs, the Berry curvature can be calculated as⁵⁹

$$\epsilon_{\alpha\beta\gamma}\Omega_{n,\gamma} = -2\text{Im} \sum_{m \neq n} \frac{\langle\langle \phi_n | \mathcal{H}_\alpha | \phi_m \rangle\rangle \langle\langle \phi_m | \mathcal{H}_\beta | \phi_n \rangle\rangle}{(\mathcal{E}_m - \mathcal{E}_n)^2}, \quad (7)$$

where $|\phi_n\rangle$ and \mathcal{E}_n are the n -th eigenvector and eigenvalue of \mathcal{H} (the 32×32 Hamiltonian matrix discussed in Sec. III), and $\epsilon_{\alpha\beta\gamma}$ is the Levi-Civita symbol, though no sum over γ is implied. Then we calculate the Chern number or Berry curvature flux χ_n of each Weyl node W_n by enclosing it in spheres of successively smaller radius,

$$\chi_n = \frac{1}{2\pi} \oint_S dS \hat{\mathbf{n}} \cdot \mathbf{\Omega}_n(\mathbf{k}), \quad (8)$$

where S is the two-dimensional surface of the sphere, or, as relevant later, S_n is the Fermi surface (FS) sheet of band n , and $\hat{\mathbf{n}}$ is a unit vector normal to S or S_n . Our calculation shows that the four Weyl nodes consist of two Weyl nodes with $\chi_n = \pm 1$ and two nodes with $\chi_n = \pm 2$. The former (latter) nodes are referred to as single (double) Weyl nodes. The Berry curvature vector fields for the single and double Weyl nodes are shown in Fig. 6(d) and (e). The calculated Chern numbers agree with the expected dispersion around the nodes. The bands forming the single Weyl nodes disperse linearly in all directions around the nodes. For the double Weyl nodes, the bands disperse linearly along the z -axis (rotational axis) and quadratically in the xy -plane. The positions, energies, and chiralities of the Weyl nodes are listed in Table II. One pair of single and double Weyl nodes, W_{25} ($\chi_{25} = -1$) and $W_{24,a}$ ($\chi_{24,a} = -2$), are located at higher energies, while the other two nodes, W_{23} ($\chi_{23} = +1$) and $W_{24,b}$ ($\chi_{24,b} = +2$), are found at lower energies.

Each Weyl node is the result of a crossing of bands with different rotational eigenvalues, inherited from the Dirac node in the absence of the magnetic field. For example, band crossings between $j_z = \pm 3/2$ and $j_z = \mp 1/2$ bands create double Weyl nodes, while band crossings between $j_z = \pm 3/2$ and $j_z = \pm 1/2$ produce single Weyl nodes, where j_z is the eigenvalue of the z component of the total angular momentum operator \mathbf{J} , as discussed in Refs. 26,29. We confirm that the j_z values for the crossing bands obtained from the WF-TB model agree with this analysis. The 6_3 screw symmetry allows double Weyl nodes⁵⁰. Figure 7 shows the field-dependence of the Weyl-node positions k_{z0} along the k_z axis calculated with the WF-TB model. At low \mathbf{B} fields the k_{z0}^2 values evolve linearly with field,

TABLE II: Chern number, momentum, and energy with respect to the Fermi level of the four Weyl nodes in the $z > 0$ half-BZ, where $W_{n,\alpha}$ is α -th Weyl node arising from band n , the corresponding band index shown in Fig. 9(a) and used in Eq. 10. Note that $\tilde{g}\mu_B B_z = 0.025$ eV.

$W_{n,\alpha}$	χ_n	k_z (\AA^{-1})	Energy (meV)
$W_{24,a}$	-2	0.10973	33.3
W_{25}	-1	0.09779	35.8
W_{23}	+1	0.07618	-60.4
$W_{24,b}$	+2	0.06237	-58.5

which is consistent with the Weyl-node positions obtained from the effective 4×4 model (shown below)^{26,29}. Although the single Weyl nodes induced by \mathbf{B} field were reported in the literature^{26,28}, the existence of the double Weyl nodes was rarely mentioned²⁹. The double Weyl nodes are realized only when an effective 4×4 effective $\mathbf{k} \cdot \mathbf{p}$ model (shown below) includes cubic terms in k , such as $B(\mathbf{k}) = -\frac{1}{2}B_3k_-^2k_z$. This $B(\mathbf{k})$ term respects the crystal symmetries and it couples the $j_z = \pm 3/2$ and $j_z = \mp 1/2$ bands, where k_{\pm} denote $k_x \pm ik_y$. The Hamiltonian reads

$$H_{4 \times 4} = \epsilon_0(\mathbf{k}) + \begin{pmatrix} M(\mathbf{k}) & A(\mathbf{k}) & 0 & B^*(\mathbf{k}) \\ A^*(\mathbf{k}) & -M(\mathbf{k}) & B^*(\mathbf{k}) & 0 \\ 0 & B(\mathbf{k}) & M(\mathbf{k}) & -A^*(\mathbf{k}) \\ B(\mathbf{k}) & 0 & -A(\mathbf{k}) & -M(\mathbf{k}) \end{pmatrix}, \quad (9)$$

where $M(\mathbf{k}) = M_0 + M_1k_z^2 + M_2(k_x^2 + k_y^2)$, $A(\mathbf{k}) = ik_+A_0(1 + A_1k_z^2 + A_2(k_x^2 + k_y^2))$, and $\epsilon_0(\mathbf{k}) = C_0 + C_1k_z^2 + C_2(k_x^2 + k_y^2)$. The parameter values except for B_3 , A_1 , and A_2 are found in Ref. 26. Note that the above Hamiltonian is in our global coordinates, where our x and y coordinates are reversed from those in Ref. 26. Since the cubic terms [$B(\mathbf{k})$, $iA_0A_1k_+k_z^2$, and $iA_0A_2k_+(k_x^2 + k_y^2)$] do not affect the linear dispersion near the Dirac nodes in zero \mathbf{B} field, the existence of the terms cannot be shown from the fitting to the DFT-calculated bands in previous studies²⁶. Our finding of the double Weyl nodes is the first direct evidence of the existence of the $B(\mathbf{k})$ term.

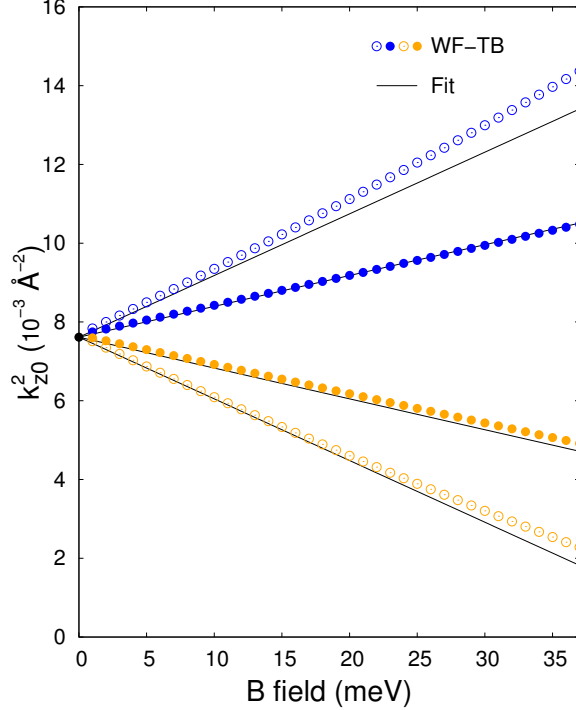


FIG. 7: (Color online) Evolution of the position of the Weyl nodes calculated with the WF-TB model versus magnetic field strength. The single (double) Weyl node positions are shown as closed (open) circles, and the blue (orange) color corresponds to the negative (positive) chiral charge. The solid black lines correspond to the average of four fits which demonstrate good agreement with the 4×4 Hamiltonian, especially at low fields. The fit for the single Weyl node ($\chi_{25}=-1$) is $k_{z0}^2(B_z) = (7.613 \cdot 10^{-3} \text{ \AA}^{-2}) + (7.830 \cdot 10^{-3} (\text{eV} \cdot \text{ \AA}^2)^{-1}) \cdot B_z[\text{eV}]$. The other fitting curves are given by the appropriate choice of the sign of the slope, and the double Weyl node fits have twice the magnitude of the slope.

C. Nodal Rings Formed via Magnetic Field

In addition to the four Weyl nodes, we also observe nodal rings in the horizontal mirror plane upon \mathbf{B} field along the c axis, which is consistent with the result obtained from the effective 4×4 model²⁹. Figure 8(a) shows bands $n=21 - 24$ along the k_x (or k'_z) axis. For $\tilde{g}\mu_B B_z=5$ meV, bands 23 and 24 meet at two points along the k_x axis, while for $\tilde{g}\mu_B B_z=25$ meV, the two bands meet at four points. In the $k_x - k_y$ plane bands 23 and 24 form one nodal ring at low fields like $\tilde{g}\mu_B B_z=5$ meV but two nodal rings at higher fields like $\tilde{g}\mu_B B_z=25$ meV, as shown in Fig. 8(a) and (b). Further, we calculate a π Berry

phase on a loop-path which interlocks with one nodal ring (one path for each ring), and this demonstrates the protection of the nodal rings due to the mirror symmetry^{51,52}. Not all the gapless points at the nodal rings have the same energy. As shown in Fig. 8(c) for $\tilde{g}\mu_B B_z=25$ meV, the inner ring is more or less at the same energy, while the outer ring has some variations in the energy. This is not surprising. It has been shown in other nodal ring or line semimetals^{53,54}. A nodal ring was found in fcc bulk Fe with SOC⁵⁵. In most reported nodal ring or line semimetals, the nodal rings or lines become gapped except for a few points in the presence of SOC. However, the nodal rings persist with SOC in TRS-broken WSMs.

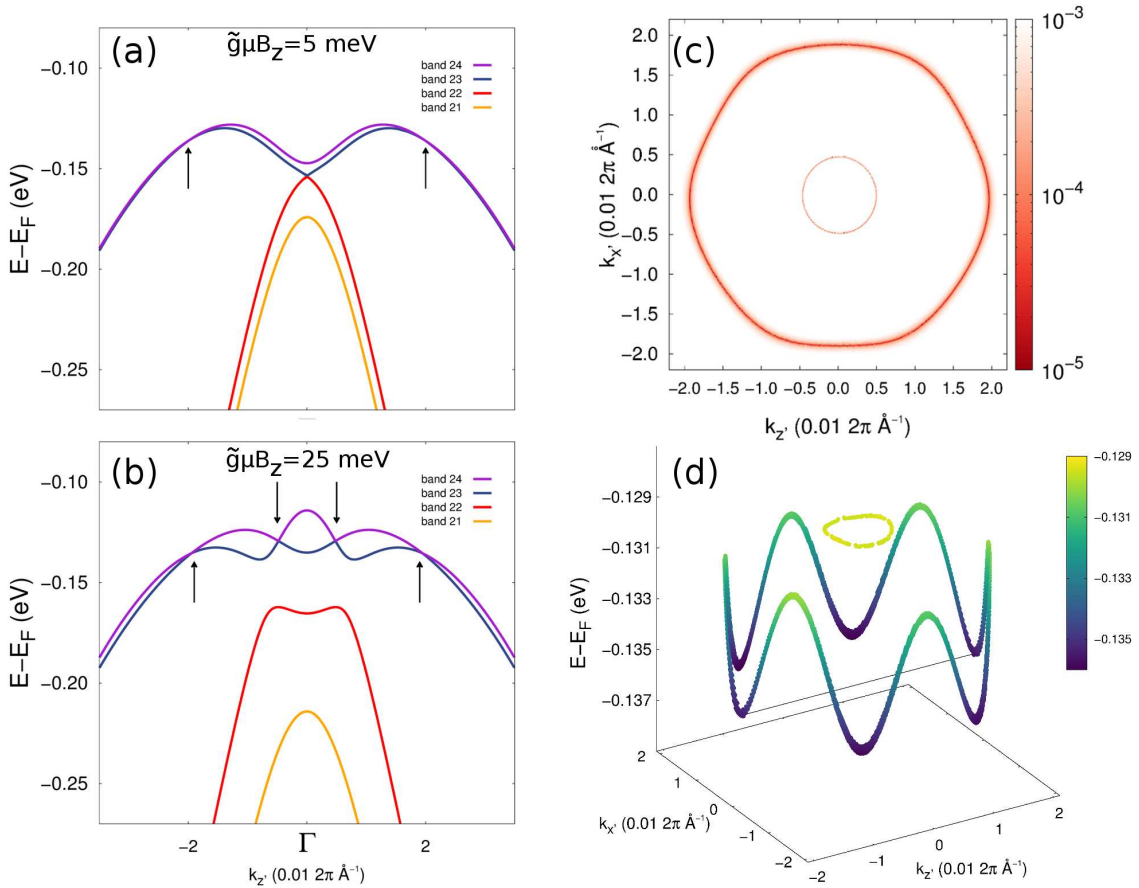


FIG. 8: (Color online) (a) Dispersion of bands 21 – 24 of Na₃Bi along the k_z' axis with $\tilde{g}\mu_B B_z=5$ meV. The gapless points are emphasized with arrows. (b) Likewise when $\tilde{g}\mu_B B_z=25$ meV. (c) Nodal rings formed by bands 23 and 24 in the $k_x - k_y$ plane for $\tilde{g}\mu_B B_z=25$ meV. The colorscale is a logscale for the size of the bandgap in eV. (d) Gapless nodal rings in the $k_x - k_y$ plane vs energy for $\tilde{g}\mu_B B_z=25$ meV. The color scale is for the energy of the bands.

D. Evolution of Fermi Arcs as a Function of Chemical Potential

We now present our calculation of Fermi arc surface states at a single surface as a function of chemical potential μ in the presence of \mathbf{B} field. As the experimental transport signatures of the Fermi arcs are strongly dependent on the chemical potential relative to the energy of the Weyl nodes, our analysis has qualitative explanatory relevance to future transport experiments involving topological Dirac semimetals in an applied magnetic field. We compute the bulk states and the surface states for a semi-infinite slab with the $(1\bar{2}0)$ surface by using an iterative Green's function method⁵⁶ as implemented in WANNIER TOOLS⁴⁹. We use three principle layers in the iterative method. Figure 9(a) shows a zoom-in of the five bands $n=22 - 26$ near the Fermi level, colored in correspondence with Fig 8 and for future reference. Figure 9(b)-(f) shows the calculated Fermi arcs at five values of chemical potential, E_1, \dots, E_5 as indicated in Fig 9(a). The Fermi arcs are indicated as red curves, while the bulk states are shown as white and pale red. The single and double Weyl points are marked as small and large circles, respectively. The orange (blue) color is for the positive (negative) chirality. Weyl nodes on the $+k_{y'}$ axis are related to the Weyl nodes on the $-k_{y'}$ axis by the horizontal mirror plane. Figure 10 shows zoom-ins of the Fermi arcs and bulk states near the Weyl points at the five energies. We denote the boundary of a Fermi surface (FS) volume \mathcal{V} of band n at different μ values as S_n . The color of the boundary in Fig. 10 corresponds to the denoted band index as in Fig. 9(a).

At $\mu=E_1=40$ meV we find two Fermi arc surface states in Fig. 9(b). One of them terminates tangentially on each of two FS sheets such as S_{26} (labeled in Fig. 10) and its mirror partner, whereas the other Fermi arc terminates tangentially on FS sheet S_{25} , as shown in Figs. 9(b) and 10(a). At both $\mu=E_2=10$ meV and $\mu=E_3=-20$ meV, we observe four Fermi arc surface states in the half-BZ; two arcs end tangentially on FS sheet S_{25} and the other two (appearing within the gap between S_{24} and S_{25}) terminate tangentially on S_{24} , as shown in Figs. 9(c) and (d) and 10(b) and (c). Figure 10(d) provides a zoom-in view of the latter two Fermi arcs, and clearly shows the gap between the two different FS sheets. This zoom-in view is qualitatively the same for $\mu=E_2$, E_3 and E_4 , discussed next. At $\mu=E_4=-50$ meV we find one surface-state loop connected through S_{25} and three Fermi arcs ending tangentially on S_{24} [Fig. 10(e) and Fig. 9(e)]. In this case, the closed surface state is similar to a topological-insulator-like surface state in external in-plane \mathbf{B} fields^{57,58},

and it terminates *non-tangentially* on S_{25} . The two Fermi arcs within the gap between S_{24} and S_{25} look similar to the cases of E_2 and E_3 . The third Fermi arc looks like a short whisker which forms off of the “crumpled-nosecone” of S_{24} and is lost into the projected bulk states. At $\mu=E_5=-65$ meV we observe one topological-insulator-like closed surface state well separated from the bulk states and one whisker-like Fermi arc terminating tangentially on $S_{23,a}$ [Fig. 10(f) and Fig. 9(f)].

E. Analysis of Fermi-Arcs Evolution from Fermi Surface Chern numbers

In order to understand the evolution of the Fermi arcs as a function of μ , we examine the Chern numbers of disjoint FS sheets at different μ values around the Weyl nodes following Gosálbez-Martínez *et al.*⁵⁵. The Chern number, C_n , of each FS sheet $S_{n,\alpha}$ enclosing a volume \mathcal{V} arising from band n is given by

$$C_n = \sum_{W_{n,\alpha} \in \mathcal{V}} \chi_{n,\alpha} - \sum_{W_{n-1,\alpha} \in \mathcal{V}} \chi_{n-1,\alpha}, \quad (10)$$

where $\chi_{n,\alpha}$ is the chirality of the α^{th} Weyl node connecting bands n and $n+1$, $W_{n,\alpha}$. The sum is over all Weyl nodes interior to the FS sheet; the outward pointing normal vector points toward the exterior of the FS for electron-pockets and the reverse for hole-pockets. With this convention, the band crossing point becomes a source of Berry curvature flux in the lower band (n) and a sink of Berry curvature flux in the upper band ($n+1$). Table III lists the calculated FS Chern numbers of each Fermi sheet belonging to each band at each of the five chemical potential values.

TABLE III: C_n for each Fermi surface sheet, S_n , as a function of chemical potential (meV). Only Fermi surface sheets appearing in the $z > 0$ (or $y' > 0$) half-BZ are listed. Not all $S_{n,\alpha}$ are shown in Fig. 9(a).

n, α in $S_{n,\alpha}$	$E_1=+40$	$E_2=+10$	$E_3=-20$	$E_4=-50$	$E_5=-65$
26	+1	-	-	-	-
25	0	0	0	0	-
24	-	+2	+2	0	0
23,a(b)	-	-	-	0	-1 (0)

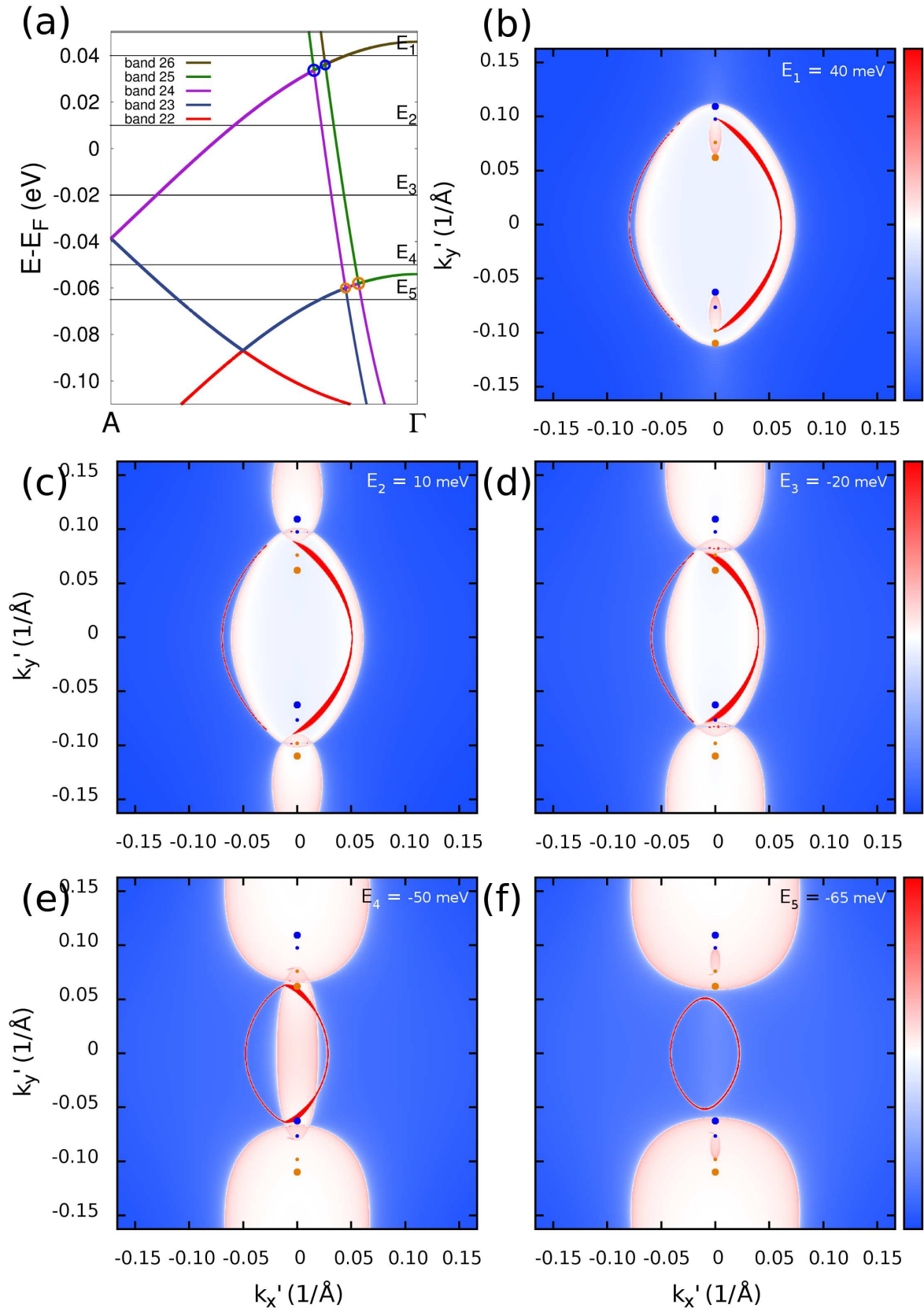


FIG. 9: (Caption on page 24.)

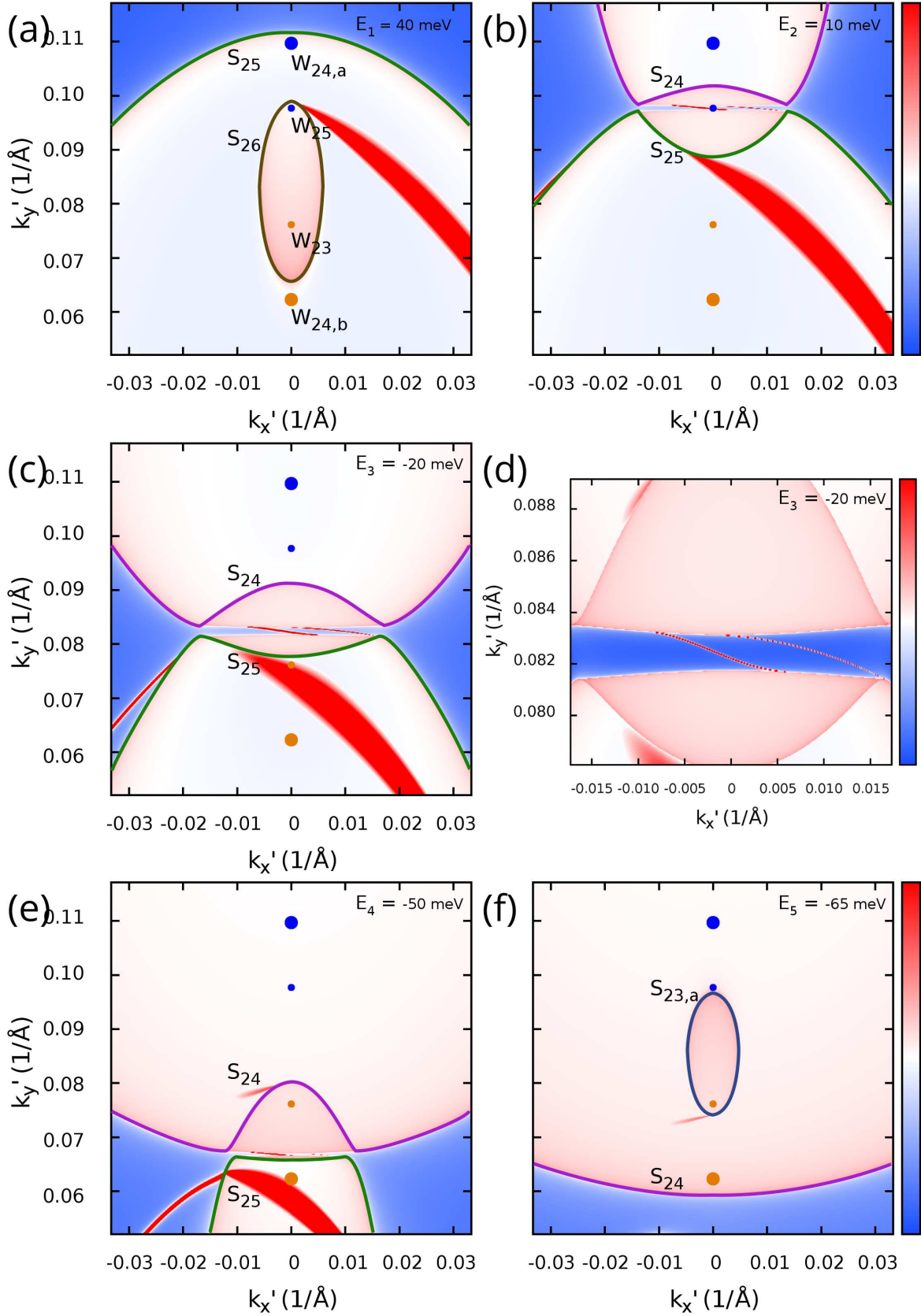


FIG. 10: (Caption on page 24.)

FIG. 9: (Color online) (a) Zoom-in on the band structure showing the five choices of chemical potential. (b-f) Fermi arcs and other surface states on the $(1\bar{2}0)$ in an area one quarter of the full BZ area. The panels show $E_1 - E_5$ respectively, which are +40, +10, -20, -50 and -65 meV. The colorscale is a chimera of the spectral densities of the bulk and surface Green's functions: significant weight of the bulk Green's function appears white or light red, and weight on the Fermi arc surface states appears as strictly the darkest red. This makes it apparent that many of the surface states attach tangentially to the bulk Fermi surface, and at low enough energy the surface states are disconnected from the bulk Fermi surface.

FIG. 10: (Color online) (a-f) Fermi arcs on the $(1\bar{2}0)$ surface, magnified near to the Weyl nodes at energies $E_1 - E_5$ respectively, which are +40, +10, -20, -50 and -65 meV. (d) is a zoom-in on the two Fermi arc states at $E_3=-20$ meV connecting the $C_{24}=+2$ and $C_{25}=0$ Fermi surface sheets. The colorscale in all panels is a chimera of the spectral densities of the bulk and surface Green's functions: significant weight of the bulk Green's function appears white or light red, and weight on the Fermi arc surface states appears as strictly the darkest red. This makes it apparent that many of the surface states attach tangentially to the bulk Fermi surface.

At $\mu=E_1$, the chemical potential meets bands 25 and 26 and so C_{25} and C_{26} are relevant to our analysis [Figs. 9(b) and 10(a)]. We find that a small electron-pocket ellipsoid $S_{26,a}$ (brown) encloses W_{25} and W_{23} . Only W_{25} enters into the calculation of C_{26} according to Eq. (10) and so FS sheet $S_{26,a}$ inherits a Chern number of $C_{26} = -\chi_{25} = +1$. The other electron-pocket ellipsoid S_{25} (green) encloses all eight Weyl nodes in the full BZ. Among them, all the Weyl nodes except for W_{23} and its mirror-symmetry partner are relevant, and its FS Chern number is zero, i.e. $C_{25}=0$. This is alternatively understood from the fact that S_{25} encloses the parity-invariant Γ point, so its Chern number must be zero. From the calculations of C_{25} and C_{26} , we might expect one Fermi arc per surface terminating on S_{26} and zero terminating on S_{25} . However, Haldane⁶⁰ points out that Fermi arcs arising from Weyl nodes higher or lower in energy may still be observed away from the energy of the Weyl node (even when the FS Chern number is zero by enclosing Weyl nodes of opposite chirality), so long as they terminate tangentially and respect the Chern number of the Fermi surface. For $C_{25}=0$, such a state would have to originate from and terminate on the same surface. This analysis agrees with the observed two Fermi arcs discussed in Sec. IV.D [Fig. 9(a)].

At $\mu=E_2$, bands 24 and 25 meet the chemical potential and so C_{24} and C_{25} are relevant to the counting of the Fermi arcs [Figs. 10(c) and 10(b)]. For S_{25} a similar analysis to the case of $\mu=E_1$ can be applied and thus $C_{25}=0$. The hole-pocket S_{24} (magenta) encloses the double Weyl node $W_{24,a}$, yielding $C_{24}=+2$. Note that an extra minus seems to enter for a hole pocket in Eq. (10), but only because of the reversed direction of the Fermi velocity vector at the surface of the hole pocket alters the sense of which Weyl nodes are *interior* to the FS sheet. One may initially expect two Fermi arcs to connect S_{24} and its mirror partner, yet these arcs terminate on S_{25} . Figure 11 represents this case schematically to facilitate discussion. Though these Fermi arcs in the $k_{y'} > 0$ half-BZ terminate on S_{25} , their mirror symmetric partner states in the $k_{y'} < 0$ half-BZ do so as well. In this sense two arcs enter and two arcs exit S_{25} , consistent with $C_{25}=0$. Meanwhile the separated hole FS sheets, S_{24} and its mirror partner, have a net flow of Fermi arcs (indicated as red arrows in Fig. 11) into or out of each and in opposite measure, consistent with their nontrivial and opposite FS Chern numbers. At $\mu=E_3$, the analysis is much the same as at the preceding energy except that the hole-pocket S_{24} encloses an extra Weyl node W_{25} [Fig. 10(c)]. The extra Weyl node connects bands with indices which are irrelevant for the calculation of the hole-pocket Chern number (C_{24}), and so C_{24} does not change.

At $\mu=E_4$, the chemical potential meets bands 23, 24, and 25, and so C_{23} , C_{24} , and C_{25} are relevant [Fig. 10(e)]. The crossing point between bands 23 and 24 at the BZ boundary (A point) does not carry any chirality and the hole-pocket S_{23} (not shown) encloses this crossing point. Thus we obtain $C_{23}=0$. The electron-pocket S_{25} encloses $W_{24,b}$ and its partner with opposite chirality across the Γ point, and so $C_{25}=0$. Now S_{24} is roughly ellipsoidal except for a “crumpled-nosecone” shape near where it avoids S_{25} . The Weyl node W_{23} is actually *exterior* to S_{24} . S_{24} extends all the way across the BZ boundary (the A point) enclosing $W_{24,a}$ and its partner with opposite chirality, so we have $C_{24}=0$. Our analysis shows that the number of Fermi arcs is not constrained at this chemical potential.

At $\mu=E_5$, bands 23 and 24 cross the chemical potential which is below the energies of all four Weyl nodes. In the half-BZ ($y' > 0$), there are two disjoint hole-pockets $S_{23,a}$ (blue) and $S_{23,b}$ (not shown in Fig. 10(f)). The former hole pocket encloses only W_{23} while the latter pocket encloses the A point, so $C_{23,a(b)}=-1(0)$. The hole-pocket S_{24} (magenta) reaches all the way across the the BZ boundary, enclosing the parity-invariant point A (not shown) and also all of the Weyl nodes and their partners. Thus $C_{24}=0$. This analysis dictates one Fermi

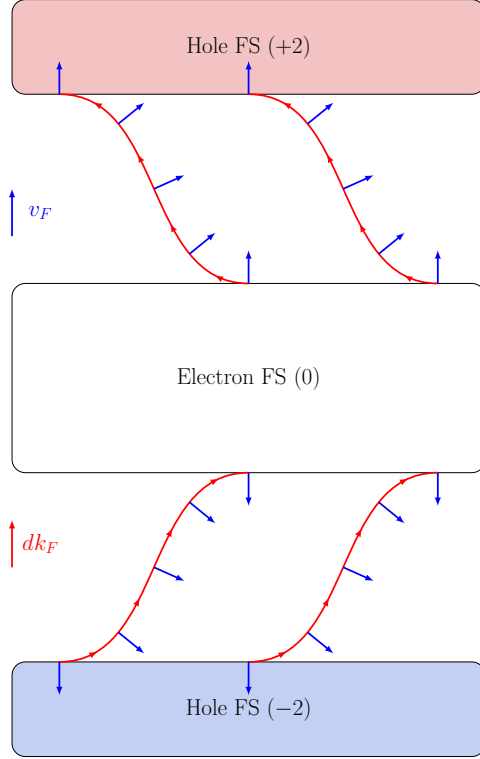


FIG. 11: (Color online) Schematic representation of the attachment of Fermi arcs in the full surface Brillouin zone. The upper-half of this figure should be compared with Fig. 10(d). The Fermi arcs on one surface attach tangentially to the Fermi surface (FS) sheets. The local Fermi velocities, v_F , (blue arrows) match at the points of attachment; pointing outward (inward) for electron (hole) pockets. Choosing a consistent direction for the differential Fermi vector, dk_F , (red arrows) along the Fermi arc as in Ref. 60 (i.e. $(\hat{n} \times \vec{v}_F) \cdot d\vec{k}_F > 0$), there is a net Fermi arc flux associated with the FS sheets with nontrivial Chern number, while such flux is zero into the FS with zero Chern number (two arcs enter and two arcs exit).

arc tangentially terminating on $S_{23,a}$, which corroborates our result.

V. CONCLUSION

In summary, we have developed a WF-TB model for the topological DSM, Na_3Bi , which reproduces the DFT-calculated band structure well while retaining the symmetries of the crystal. The projected atomic Wannier functions are atom-centered with larger spread

than maximally localized WFs. Atomic-like SOC was included, and we investigated the formation of line nodes in the mirror plane and splitting of the Dirac nodes into multiple Weyl nodes in an applied magnetic field. We found that each Dirac node splits into pairs of Weyl nodes with chiral charges ± 1 and ± 2 from the calculations of Berry curvature. By carefully considering the Chern number of associated Fermi surface sheets, we detailed the interesting development of Fermi arc and other topological surface states as a function of chemical potential consistent with the topological charges of the Weyl nodes. Our tight-binding model can be used to calculate novel properties induced by the nonzero Berry curvature, and its qualitative features can be applied in another experimentally observed topological DSM, Cd_3As_2 .

Acknowledgments

J.V. was supported by the National Science Foundation (NSF) CREST Center for Interface Design and Engineered Assembly of Low-dimensional Systems (IDEALS) under NSF grant number HRD1547830. The computational support was provided by San Diego Supercomputer Center (SDSC) under DMR060009N and VT Advanced Research Computing (ARC).

Appendix A: Electronic Structures Using the Non-primitive Unit Cell

In Fig. 3 of the main text, we compared the band structure of the WF-TB model in the non-primitive unit cell to the familiar band structure of bulk Na_3Bi calculated in the primitive unit cell. In this section, we present the band structure of Na_3Bi calculated using VASP versus the band structure calculated using the WF-TB model in the non-primitive unit cell for ease of comparison, given the band-folding. Figure 12(a) shows the bands in the non-primitive unit cell without SOC; there is excellent agreement in the whole of the valence band and up to even 1 eV above the Fermi level. Figure 12(b) shows the bands with SOC included; while far from the Fermi level the bands are identical in dispersion but differ by a vertical shift in energy, there is excellent agreement within $[-0.5, 0.5]$ eV around the Fermi level. Hence our WF-TB model reproduces the DFT electronic structure very well with and without SOC even for the non-primitive unit cell.

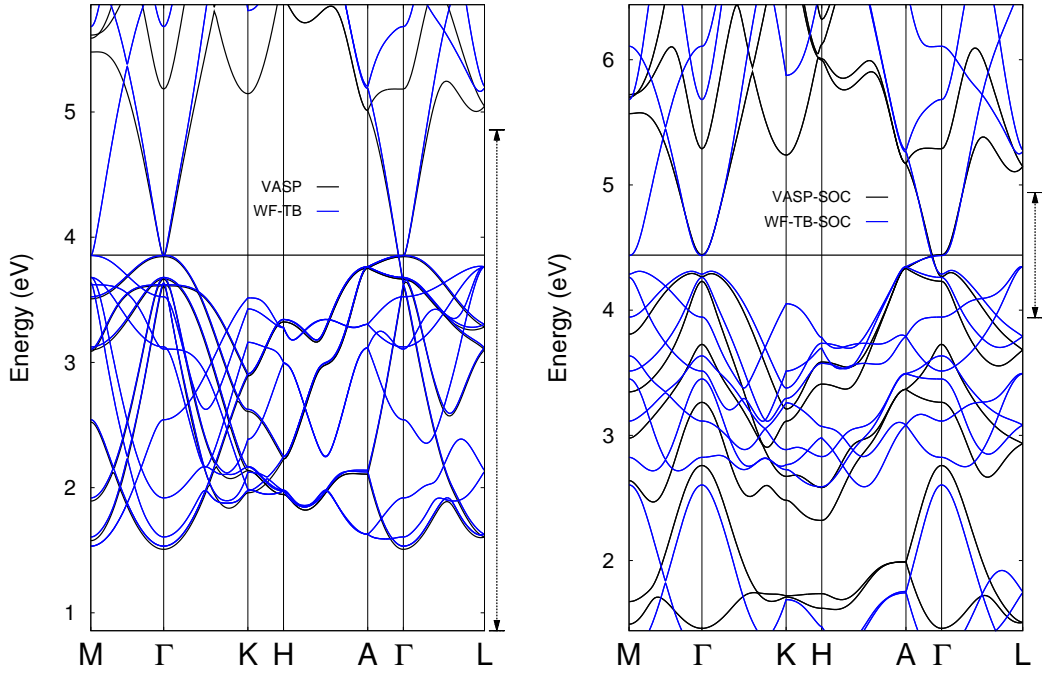


FIG. 12: (Color online) Band structures of bulk Na_3Bi in the non-primitive unit cell (a) without SOC and (b) with SOC. The black (dark) bands show the the DFT-calculated bands using VASP, and the blue (light) bands are calculated from the WF-TB model. The high-symmetry point labels correspond to those in the primitive unit cell, so the band structures clearly show band-folding, e.g. midway along $\text{M}\Gamma$ where the non-primitive unit cell BZ ends. The vertical arrows draw the eye to the region of excellent agreement referenced in the text.

* Electronic address: jwdevill@vt.edu

† Electronic address: kyungwha@vt.edu

¹ H. B. Nielsen and M. Ninomiya, Phys. Lett. B **105**, 219-223 (1981).

² X. Wan, A. M. Turner, A. Vishwanath, and S. Y. Savrasov, Phys. Rev. B **83**, 205101 (2011).

³ G. Xu, H. Weng, Z. Wang, X. Dai, and Z. Fang, Phys. Rev. Lett. **107**, 186806 (2011).

⁴ C. Fang, M. J. Gilbert, X. Dai, and B. A. Bernevig, Phys. Rev. Lett. **108**, 266802 (2012).

⁵ H. Weng, C. Fang, Z. Fang, B. A. Bernevig, and X. Dai, Phys. Rev. X **5**, 011029 (2015).

⁶ S.-M. Huang, S.-Y. Xu, I. Belopolski, C.-C. Lee, G. Chang, B. Wang, N. Alidoust, G. Bian,

- M. Neupane, C. Zhang, S. Jia, A. Bansil, H. Lin, and M. Z. Hasan, *Nature Commun.* **6** 7373 (2015).
- ⁷ S.-Y. Xu, I. Belopolski, N. Alidoust, M. Neupane, G. Bian, C. Zhang, R. Sankar, G. Chang, Z. Yuan, C.-C. Lee, S.-M. Huang, H. Zheng, J. Ma, D. S. Sanchez, B. Wang, A. Bansil, F. Chou, P. P. Shibayev, H. Lin, S. Jia, and M. Z. Hasan, *Science* **349**, 613-617 (2015).
- ⁸ B. Q. Lv, H. M. Weng, B. B. Fu, X. P. Wang, H. Miao, J. Ma, P. Richard, X. C. Huang, L. X. Zhao, G. F. Chen, Z. Fang, X. Dai, T. Qian, and H. Ding, *Phys. Rev. X* **5**, 031013 (2015).
- ⁹ L. X. Yang, Z. K. Liu, Y. Sun, H. Peng, H. F. Yang, T. Zhang, B. Zhou, Y. Zhang, Y. F. Guo, M. Rahn, D. Prabhakaran, Z. Hussain, S.-K. Mo, C. Felser, B. Yan, and Y. L. Chen, *Nat. Phys.* **11**, 728-732 (2015).
- ¹⁰ C. Fang, M. J. Gilbert, X. Dai, and B. A. Bernevig, *Phys. Rev. Lett.* **108**, 266802 (2012).
- ¹¹ D. Zhang, H. Wang, J. Ruan, G. Yao, and H. Zhang, *Phys. Rev. B* **97**, 195139 (2018).
- ¹² A. A. Soluyanov, D. Gresch, Z. Wang, Q. S. Wu, M. Troyer, X. Dai, and B. A. Bernevig, *Nature* **527**, 495-498 (2015).
- ¹³ P. Li, Y. Wen, X. He, Q. Zhang, C. Xia, Z.-M. Yu, S. A. Yang, Z. Zhu, H. N. Alshareef, and X.-X. Zhang, *Nat. Commun.* **8**, 2150 (2017).
- ¹⁴ D. T. Son and N. Yamamoto, *Phys. Rev. Lett.* **109**, 181602 (2012).
- ¹⁵ D. T. Son and B. Z. Spivak, *Phys. Rev. B* **88**, 104412 (2013).
- ¹⁶ A. A. Burkov, *J. Phys.: Condens. Matter* **27**, 113201 (2015).
- ¹⁷ G. Sharma, P. Goswami, and S. Tewari, *Phys. Rev. B* **93**, 035116 (2016).
- ¹⁸ G. Sharma, C. Moore, S. Saha, and S. Tewari, *Phys. Rev. B* **96**, 195119 (2017).
- ¹⁹ A. C. Potter, I. Kimchi, and A. Vishwanath, *Nat. Commun.* **5**, 5161 (2014).
- ²⁰ P. J. W. Moll, N. L. Nair, T. Helm, A. C. Potter, I. Kimchi, A. Vishwanath, and J. G. Analytis, *Nature* **535**, 266-270 (2016).
- ²¹ S. Huang, J. Kim, W. A. Shelton, E. W. Plummer, and R. Jin, *Proc. Natl. Acad. Sci. USA* **114**, 6256-6261 (2017).
- ²² M. Sato and Y. Ando, *Rep. Prog. Phys.* **80**, 076501 (2017).
- ²³ B.-J. Yang and N. Nagaosa, *Nat. Commun.* **5**, 4898 (2014).
- ²⁴ Z. K. Liu, J. Jiang, B. Zhou, Z. J. Wang, Y. Zhang, H. M. Weng, D. Prabhakaran, S.-K. Mo, H. Peng, P. Dudin, T. Kim, M. Hoesch, Z. Fang, X. Dai, Z. X. Shen, D. L. Feng, Z. Hussain, and Y. L. Chen, *Nat. Mater.* **13**, 677-681 (2014).

- ²⁵ Z. K. Liu, B. Zhou, Y. Zhang, Z. J. Wang, H. M. Weng, D. Prabhakaran, S.-K. Mo, Z. X. Shen, Z. Fang, X. Dai, Z. Hussain, Y. L. Chen, *Science* **343**, 864-867 (2014).
- ²⁶ Z. Wang, Y. Sun, X.-Q. Chen, C. Franchini, G. Xu, H. Weng, X. Dai, and Z. Fang, *Phys. Rev. B* **85**, 195320 (2012).
- ²⁷ Z. Wang, H. Weng, Q. Wu, X. Dai, and Z. Fang, *Phys. Rev. B* **88**, 125427 (2013).
- ²⁸ E. V. Gorbar, V. A. Miransky, I. A. Shovkovy, and P. O. Sukhachov, *Phys. Rev. B* **91**, 235138 (2015).
- ²⁹ J. Cano, B. Bradlyn, Z. Wang, M. Hirschberger, N. P. Ong, and B. A. Bernevig, *Phys. Rev. B* **95**, 161306(R) (2017).
- ³⁰ A. A. Soluyanov and D. Vanderbilt, *Phys. Rev. B* **83**, 035108 (2011).
- ³¹ T. Thonhauser and D. Vanderbilt, *Phys. Rev. B* **74**, 235111 (2006).
- ³² W. Zhang, R. Yu, H.-J. Zhang, X. Dai, and Z. Fang, *New J. Phys.* **12** 065013 (2010).
- ³³ R. Yu, H. Weng, Z. Fang, X. Dai, and X. Hu, *Phys. Rev. Lett.* **115**, 036807 (2015).
- ³⁴ J. W. Villanova, E. Barnes, and K. Park, *Nano Lett.* **17**, 963-972 (2017).
- ³⁵ G. Kresse and D. Joubert, *Phys. Rev. B* **59**, 1758 (1999).
- ³⁶ P. Giannozzi *et al.*, *J. of Physics: Condens. Matt.* **29**, 465901 (2017).
- ³⁷ A. A. Mostofi, J. R. Yates, G. Pizzi, Y. S. Lee, I. Souza, D. Vanderbilt, and N. Marzari, *Comput. Phys. Commun.* **185**, 2309 (2014).
- ³⁸ P. E. Blöchl, *Phys. Rev. B* **50**, 17953 (1994).
- ³⁹ J. P. Perdew, K. Burke, and M. Ernzerhof, *Phys. Rev. Lett.* **77**, 3865 (1996).
- ⁴⁰ E. Küçükbenli, M. Monni, B. I. Adetunji, X. Ge, G. A. Adebayo, N. Marzari, S. de Gironcoli, and A. Dal Corso, arXiv:1404.3015 (2014).
- ⁴¹ G. H. Wannier, *Phys. Rev.* **52**, 191 (1937).
- ⁴² N. Marzari and D. Vanderbilt, *Phys. Rev. B* **56**, 12847 (1997).
- ⁴³ I. Souza, N. Marzari, and D. Vanderbilt, *Phys. Rev. B* **65**, 035109 (2001).
- ⁴⁴ D. J. Thouless, *J. Phys. C* **17**, L325 (1984).
- ⁴⁵ J. I. Mustafa, S. Coh, M. L. Cohen, and S. G. Louie, *Phys. Rev. B* **94**, 125151 (2016).
- ⁴⁶ W. Zhang, R. Yu, H.-J. Zhang, X. Dai, and Z. Fang, *New J. Phys.* **12** 065013 (2010).
- ⁴⁷ J. Xiong, S. K. Kushwaha, T. Liang, J. W. Krizan, M. Hirschberger, W. Wang, R. J. Cava, and N. P. Ong, *Science* **350**, 413-416 (2015).
- ⁴⁸ S. Jeon, B. B. Zhou, A. Gyenis, B. E. Feldman, I. Kimchi, A. C. Potter, Q. D. Gibson, R. J.

- Cava, A. Vishwanath, and A. Yazdani, *Nat. Mat.* **13**, 851-856 (2014).
- ⁴⁹ Q. Wu, S. Zhang, H.-F. Song, M. Troyer, and A. A. Soluyanov, *Comput. Phys. Commun.* **224**, 405-416 (2017).
- ⁵⁰ S. S. Tsirkin, I. Souza, and D. Vanderbilt, *Phys. Rev. B* **96**, 045102 (2017).
- ⁵¹ Y.-H. Chan, C.-K. Chiu, M. Y. Chou, and A. P. Schnyder, *Phys. Rev. B* **93**, 205132 (2016).
- ⁵² D. Vanderbilt and R. D. King-Smith, *Phys. Rev. B* **48**, 4442 (1993).
- ⁵³ Q. Xu, R. Yu, Z. Fang, X. Dai, and H. Weng, *Phys. Rev. B* **95**, 045136 (2017).
- ⁵⁴ Y. Quan, Z. P. Yin, and W. E. Pickett, *Phys. Rev. Lett.* **118**, 176402 (2017).
- ⁵⁵ D. Gosálbez-Martínez, I. Souza, and D. Vanderbilt, *Phys. Rev. B* **92**, 085138 (2015).
- ⁵⁶ M. P. López Sancho, J. M. López Sancho, and J. Rubio, *J. Phys. F: Met. Phys.* **15**, 851-858 (1985).
- ⁵⁷ A. A. Zyuzin, M. D. Hook, and A. A. Burkov, *Phys. Rev. B* **83**, 245428 (2011).
- ⁵⁸ S. S. Pershoguba and V. M. Yakovenko, *Phys. Rev. B* **86**, 165404 (2012).
- ⁵⁹ X. Wang, J. R. Yates, I. Souza, and D. Vanderbilt, *Phys. Rev. B* **74**, 195118 (2006).
- ⁶⁰ F. D. M. Haldane, arXiv:1401.0529v1 (2014).